Optics Communications 577 (2025) 131339

Contents lists available at ScienceDirect

Optics Communications

journal homepage: www.elsevier.com/locate/optcom

Liquid metal-based reconfigurable linear-to-multi-polarization conversion metasurfaces

Shibo Gao [a,b,c], Bowen Li [a,c], Yu Lin [a,c], Yanan Shao [a,b,c], Yongting Deng [a], Jan G. Korvink [d,*], Yongbo Deng [d,*]

[a] Changchun Institute of Optics, Fine Mechanics and Physics (CIOMP), Chinese Academy of Sciences, Changchun, 130033, China
[b] University of Chinese Academy of Sciences, Beijing, 100039, China
[c] State Key Laboratory of Applied Optics, Changchun Institute of Optics, Fine Mechanics and Physics, Chinese Academy of Sciences, Changchun, 130033, China
[d] Institute of Microstructure Technology (IMT), Karlsruhe Institute of Technology (KIT), Hermann-von-Helmholtzplatz 1, Eggenstein-Leopoldshafen, 76344, Germany

ARTICLE INFO

Keywords:
Liquid metal
Metasurface
Microfluidics
Polarization conversion
Reconfigurable metasurface

ABSTRACT

Metasurfaces as advanced artificial materials enable a variety of electromagnetic control functions, especially polarization manipulation. The existing functional switching methods tend to produce a high system complexity and encounter challenges, such as limited working bandwidth and insufficient reconfigurable degrees of freedom, although polarization conversion device based on reconfigurable metasurfaces are extensively investigated. Here, we propose a multifunctional polarization converter employing a liquid metal-based metasurface with various types of integrated microchannels on a single layer. The switching among different functionalities occurs through the injection of liquid metal into various types of microfluidic channels, maintaining the electromagnetic performance of the polarization converter, which encompasses broadband capability and large insensitivity of incident angle. Metasurfaces based on liquid metal microfluidic technology present highly adaptable and reconfigurable materials, offering new possibilities for the development of electromagnetic devices with unprecedented flexibility, with potential applications in microwave imaging, communication systems, remote sensing, among others.

1. Introduction

Metasurfaces are engineered surfaces that offer significant advantages in manipulating electromagnetic waves. By manipulating the electromagnetic characteristics, a wide range of intriguing applications can be realized, including beam deflection [1,2], beam scanning [3], beam splitting [4,5], flat lenses [6,7], holograms [8,9], microwave imaging [10,11], retroreflector [12,13], and more. Furthermore, metasurface provides a promising approach for controlling polarization states due to its capability to induce sudden alterations in the amplitude and phase of electromagnetic waves [14,15].

However, many existing metasurface-based polarizers utilize fixed unit cells, resulting in limited operating bandwidth and a single conversion mode. This limitation presents a challenge in meeting the growing demand for versatile multifunctional devices and communications. To address the above limitations, many reconfigurable systems have been reported to achieve flexible regulation of device functions. These include mechanical rotation [16,17], integrated varactor diodes [18,19], integrated positive-intrinsic-negative (PIN) diodes [20–25], and integrated microelectromechanical system (MEMS) based switches [26–28]. In [16], a polarization reconfigurable antenna using a slot antenna and metasurface is presented, where polarization is reconfigured by rotating the metasurface. It operates around 3.5 GHz, with a fractional operating bandwidth of 11.4%. In [19], an active polarization conversion metasurface integrated with varactor diodes is proposed. By adjusting the bias voltage, the electromagnetic response of the metasurface can be tuned. With a bias voltage of 0 V, it can convert linear-polarized waves to cross-polarized waves in the frequency range of 3.9 to 7.9 GHz, and with a bias of −19 V, it functions as a circular polarization converter in the frequency range of 4.9 to 8.2 GHz. In [20], a reconfigurable polarization conversion metasurface based on PIN diodes is proposed, which switches between conversion and reflection modes by toggling the PIN diodes. In conversion mode, the metasurface reflects linearly polarized waves with 90° polarization rotation, achieving a conversion ratio of over 88% in the frequency range of 3.39 to 5.01 GHz for x- and y-polarized waves. In reflection mode, it behaves like a metal plate, with co-polarization reflection greater than −1 dB from 3.83 to 4.74 GHz. These reconfigurable approaches offer

* Corresponding authors.
E-mail addresses: jan.korvink@kit.edu (J.G. Korvink), yongbo.deng@kit.edu (Y. Deng).

https://doi.org/10.1016/j.optcom.2024.131339
Received 11 October 2024; Received in revised form 19 November 2024; Accepted 21 November 2024
Available online 28 November 2024

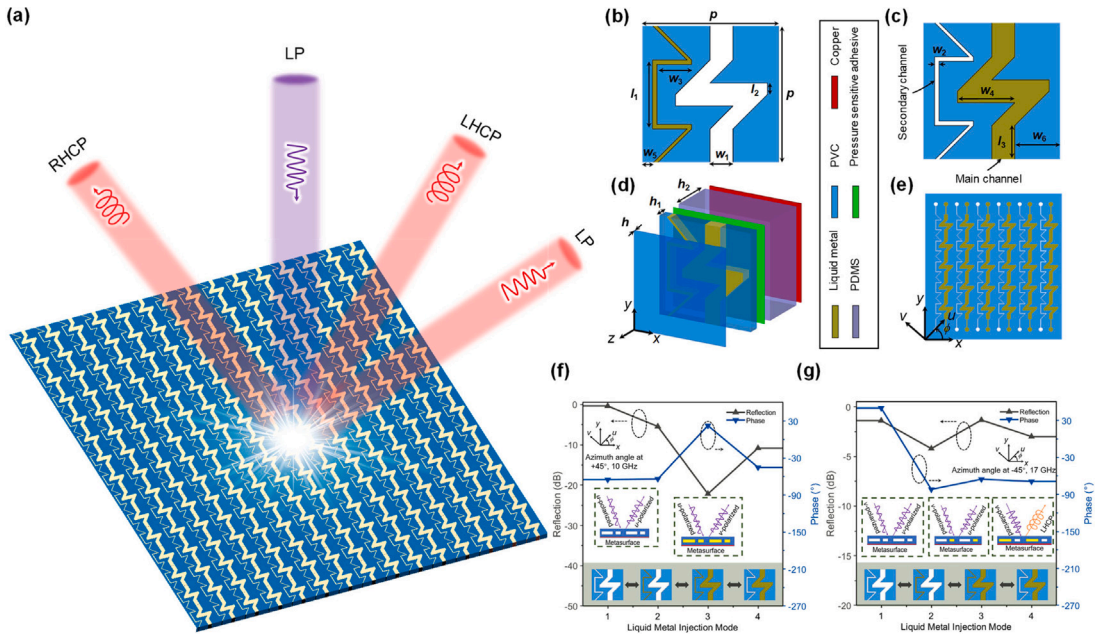

Fig. 1. Sketches for the liquid metal based microfluidic metasurface. (a) The overview of the polarization converter, leveraging an elaborately designed metasurface. (b) Unit cell in the LTLP conversion states. (c) Unit cell in the linear-to-circular polarization conversion states. (d) Exploded sketch of the unit cell. (e) Z-direction view of the array structure. (f) Simulated results for the metasurface with different injection mode in the case of *u*-polarized incident waves. (g) Simulated results for the metasurface with different injection mode in the case of *v*-polarized incident waves. Size parameters (mm): $p = 6$, $l_1 = 3$, $l_2 = 0.5$, $l_3 = 1.5$, $w_1 = 1$, $w_2 = 0.2$, $w_3 = 1.5$, $w_4 = 2.5$, $w_5 = 0.5$, $w_6 = 2$, $h = 0.5$, $h_1 = 0.9$, $h_2 = 3$.

the flexibility to adjust the functionality of metasurfaces, significantly enhancing their versatility and range of capabilities. However, implementing these techniques often necessitates the integration of direct current (DC) bias elements, which can lead to crosstalk between DC and microwave signals, thus affecting the performance of the metasurfaces. Furthermore, the inclusion of DC bias elements tends to increase the overall size of the systems, especially in scenarios where complex control demands numerous wires, which exacerbates these challenges even further. Recently, liquid-based metasurfaces have been demonstrated utilizing water, liquid crystal, and liquid metal, serving as perfect absorbers [29], tunable flat lens [30], wavefront modulators [31], adaptive retroreflectors [32], and tunable polarization converters [33, 34].

However, there is still a lack of liquid metal microfluidic metasurfaces that integrate numerous distinct microchannels on a single layer. To delve deeper into the exploration of integrated and versatile polarization converters, we introduce a reconfigurable metasurface utilizing liquid metal microfluidics for linear-to-multipolarization conversion. As a proof of the concept, a multifunctional polarization converter is demonstrated, enabling linear-to-linear polarization (LTLP), linear-to-left-hand circular polarization (LTLHCP), and linear-to-right-hand circular polarization (LTRHCP) conversions through the infusion of liquid metal into two distinct types of microfluidic channels.

2. Design and numerical results

The design and numerical simulation of the liquid metal-based reconfigurable linear-to-multi-polarization conversion metasurfaces are provided in this section.

2.1. Design of the metasurface

The elements of the liquid metal based metasurface are illustrated in Fig. 1, comprising two parts: the main microchannels with Z-shaped unit cells and secondary microchannels in a meandering configuration. By modifying the filling states of the microfluidic channels, the polarization state of the reflected waves can be flexibly regulated. As shown in Fig. 1a, when the incident wave is linearly polarized, the reflected wave from the metasurface exhibits multiple polarization states, including linear polarization (LP), left-hand circular polarization (LHCP), and right-hand circular polarization (RHCP). To facilitate these capabilities, the structure was designed with two types of microfluidic channels, as illustrated in Figs. 1b and 1c. The main and secondary microchannels measure 1 mm and 0.2 mm in width, respectively. The metasurface structure, illustrated in Fig. 1d, comprises three flexible layers. The functional layer and encapsulation layer are composed of Polyvinyl Chloride (PVC), which serves as the housing for microfluidic channels in the metasurface structure. The PVC materials has a relative permittivity ε_r of 2.4 and a loss tangent ($\tan\delta$) of 0.001. The substrate layer is constructed from grounded Polydimethylsiloxane (PDMS) and has a relative permittivity ε_r of 2.9 and a $\tan\delta$ of 0.037. The liquid metal alloy is chosen as Galinstan, consist of 68.5% gallium, 21.5% indium, and 10% tin. The Galinstan, with a low melting point of 6 °C, maintains excellent fluidity at room temperature and exhibits a conductivity of 3.46×10^6 S/m (at 20 °C), meeting the requirements of modern communication systems for metal materials. Fig. 1e presents the functional layer of the proposed metasurface, characterized by a periodic arrangement of unit cells. The process of infusing liquid metal into an array of microchannels leads to the creation of unique unit formations, consequently enabling a variety of electromagnetic responses. As shown in Table 1, working state 1 is the reflection state, corresponds to all microfluidic channels being empty without any injected liquid metal. Working states 2 and 3 involve LTLP achieved by injecting liquid metal into secondary channels and all channels of the metasurface, respectively. Working states 4 and 5 are characterized by linear-to-circular polarization, achieved by filling only the main channels with liquid metal. The metasurface can achieve functional switching within a few seconds. Specifically, the volumes of the main channel and secondary channel are 157.5 μL and 32.4 μL, respectively. When the flow rates of the syringe pump are set to 71.6 μL/s and 15 μL/s, the time required for the liquid metal to be injected into or withdrawn from the microchannels is approximately 2.2 s.

To further reveal the influence of the design parameters, Fig. 2 shows how the electromagnetic response of the metasurface varies

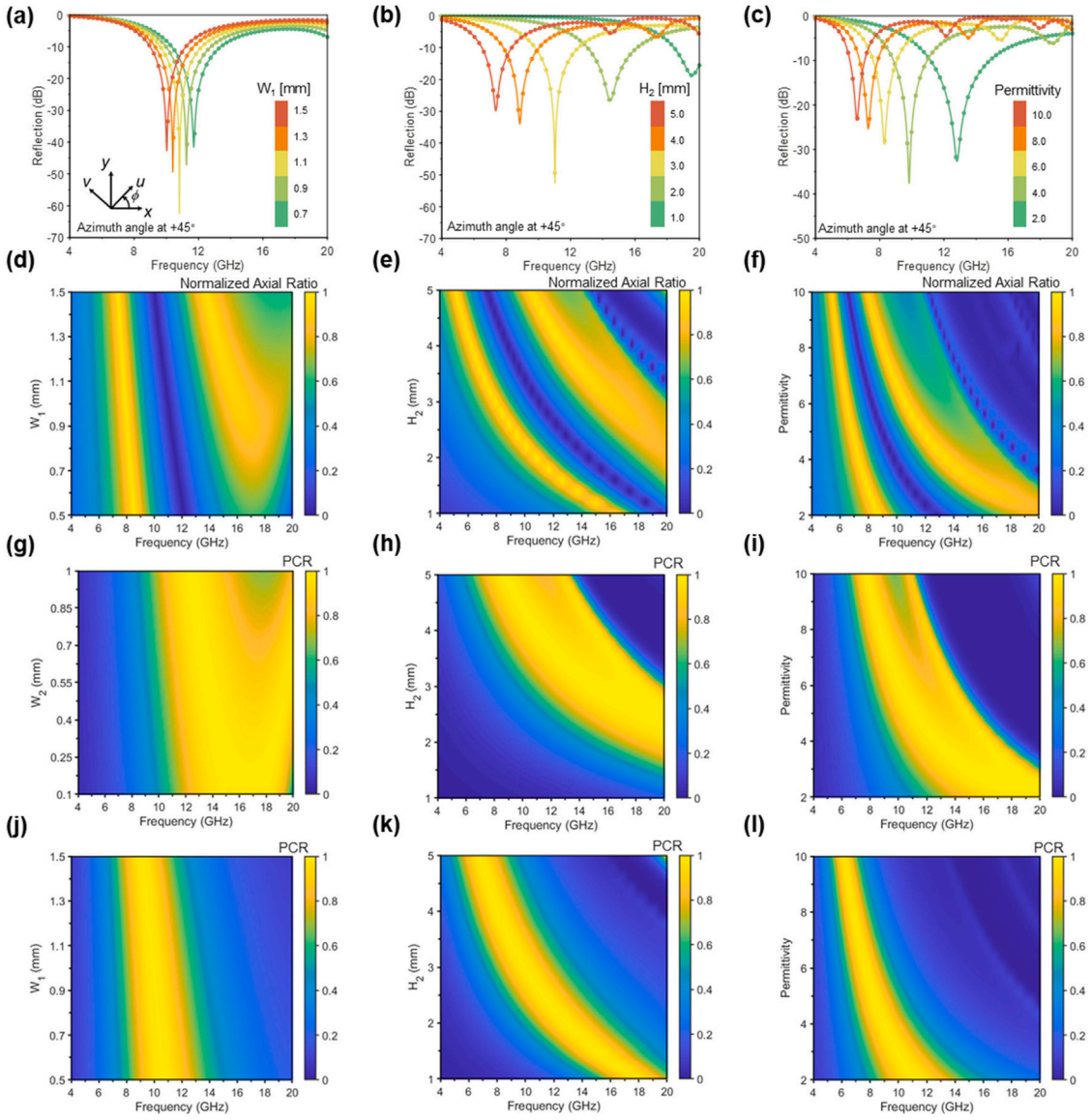

Fig. 2. Effect of the design parameters on metasurface function. (a)–(c) Presentation of the reflection amplitudes of working state 4 concerning microchannel width, dielectric layer thickness, and permittivity. (d)–(f) Presentation of the polarization conversion capability of working state 4 with respect to microchannel width, dielectric layer thickness, and permittivity. (g)–(i) Presentation of the polarization conversion capability of working state 2 with respect to microchannel width, dielectric layer thickness, and permittivity. (j)–(l) Presentation of the polarization conversion capability of working state 3 with respect to microchannel width, dielectric layer thickness, and permittivity.

Table 1
Materials arrangement for different working state.

State No.	Azimuth angle	Main channel	Secondary channel	Working state	Liquid metal volume
1	Arbitrary ϕ	Air	Air	Reflection	0 μL
2	$\phi = \pm 45°$	Air	Galinstan	LTLP	32.4 μL
3	$\phi = \pm 45°$	Galinstan	Galinstan	LTLP	189.9 μL
4	$\phi = +45°$	Galinstan	Air	LTRHCP	157.5 μL
5	$\phi = -45°$	Galinstan	Air	LTLHCP	157.5 μL

with the design parameters under different working states. In Figs. 2a–2c, the reflection amplitude in the working state 4 is investigated as a function of the microchannel width, dielectric layer thickness, and permittivity, respectively. As shown in Fig. 2a, as w_1 increases, the resonant point of the reflection amplitude moves to low frequency. This phenomenon can be explained by the equivalent circuit theory. The increase of the linewidth of the microchannel reduces the spacing between the two adjacent metal structures, which leads to the increase of the equivalent capacitance, and then the resonant frequency is reduced. Similar results can also be observed in Figs. 2d, 2g and 2j. Commonly used evaluation indexes for electromagnetic wave polarization conversion performance are polarization conversion ratio (PCR) and axial ratio. Numerical calculation results in Fig. 2d show that with the increase of w_1, the peak value of normalized axial ratio moves to the low frequency, and the bandwidth decreases significantly in the high frequency region. As shown in Fig. 2b, the dielectric layer thickness (h_2), as an important dimensional parameter, also has a significant impact on the function of the metasurface. When h_2 increases from 1 mm to 5 mm, the resonant point of the reflection amplitude shifts significantly, decreasing from 19.55 GHz (K-Band) to 7.37 GHz

(C-band), with a bandwidth of 90.49%. Similar results can also be observed in Figs. 2e, 2h and 2k. The microstructure of the metasurface can be equivalent to the local resonant cavity, because the wavelength of the electromagnetic wave is positively correlated with the size of the resonator, and the thickening of the dielectric layer can match longer wavelengths, so that the resonant frequency is reduced. This sensitivity to the dielectric thickness is beneficial to the development of ultra-wideband electromagnetic devices. In addition, the relevant parameters of materials, such as permittivity, are also important design parameters of metasurfaces. The increase of dielectric constant is equivalent to the increase of metasurface equivalent capacitance, resulting in the decrease of resonant frequency. Figs. 2c, 2f, 2i and 2l all confirm the negative correlation between dielectric constant and resonant frequency. Fig. 2 explores the impact of design parameters under an incident azimuth of +45°. Given the structural symmetry, analogous results are observed under an incident azimuth of −45°. Supplementary explanations are provided in Figures S1–S4 to further elucidate these findings. The above analysis demonstrates that combining the rational selection of materials with the optimization of design parameters can meet various functional requirements, thereby enhancing the design versatility and functional diversity of metasurfaces.

2.2. Polarization conversion mechanism

As shown in Fig. 1e, the u-polarized incident wave can be decomposed into two orthogonal components $\mathbf{E}_{ix}$ and $\mathbf{E}_{iy}$ in the x- and y-directions, respectively. Those two components have equal amplitude and phase. The electric field of the incident wave can be expressed as

$$\mathbf{E}_i = \frac{\sqrt{2}}{2}(\mathbf{e}_x E_0 e^{jkz} + \mathbf{e}_y E_0 e^{jkz}), \tag{1}$$

where $\mathbf{e}_x$ and $\mathbf{e}_y$ are the unit vectors in the x- and y-directions respectively, k is the wave number of the incident electromagnetic waves, E_0 denotes the amplitude of the incident wave $\mathbf{E}_i$; and z is the vertical coordinate. The output of the polarization converter can be described as

$$\mathbf{E}_r = \frac{\sqrt{2}}{2} E_0(\mathbf{e}_x \left|R_{xx}\right| e^{-j(kz+\varphi_{xx})} + \mathbf{e}_y \left|R_{yy}\right| e^{-j(kz+\varphi_{yy})}), \tag{2}$$

where $\left|R_{xx}\right|$ and $\left|R_{yy}\right|$ are the amplitudes of the reflected wave under x- and y-polarized wave excitations, respectively. φ_{xx} and φ_{yy} are the phases of the reflected waves under x- and y-polarized incident waves, respectively. Based on the electromagnetic theory, the reflected wave retains its u-polarization once $|R_{xx}| = |R_{yy}|, \Delta\varphi = \varphi_{xx} - \varphi_{yy} = 0°$ are satisfied, where $\Delta\varphi$ represents the phase difference between the waves reflected with x- and y-polarization. If we want to realize the LTLP conversion from u-to-v polarization, we should have $|R_{xx}| = |R_{yy}|, \Delta\varphi = \varphi_{xx} - \varphi_{yy} = \pm 180°$. Similarly, if we want to realize the linear-to-circular polarization conversion, we should have $|R_{xx}| = |R_{yy}|, \Delta\varphi = \varphi_{xx} - \varphi_{yy} = \pm 90°$.

2.3. Simulation and analysis

The multifunctional polarization converter is analyzed by solving Maxwell's equations utilizing the finite-integration technique (FIT) while enforcing periodic boundary conditions. The unit cells are exposed to incident electromagnetic waves of either u- or v-polarization originating from the z-direction.

In order to ascertain the functionality of the designed metasurface, reflection amplitudes were simulated for incident waves polarized in the u- and v-directions, respectively. Here, $|R_{uu}| = |E_{ru}|/|E_{iu}|$ is defined as the amplitude of the co-polarized reflection coefficient, where the first and second subscripts of R indicate the polarization direction of the reflected and incident electromagnetic waves, respectively. The symbol E represents the electric field, with the subscripts i and r denoting incident and reflected electromagnetic waves, respectively, and the second subscript of E representing the polarization direction. Similarly, $|R_{vu}| = |E_{rv}|/|E_{iu}|$ denotes the amplitude of the cross-polarized reflection coefficient. The polarization conversion performance of the metasurface can be assessed by simulating the S-parameters under various filling states. The reflection coefficients of the working states 2 and 3 are shown in Figs. 3a and 3b, respectively. These simulation results depict the reflected wave characteristics under the excitation of a u-polarized incident wave. Upon analyzing Figs. 3a and 3b, it becomes evident that the cross-polarized reflection coefficient R_{vu} exhibits a significantly higher amplitude compared to the co-polarized reflection coefficient R_{uu}. In Figs. 3a and 3b, R_{uu} drops below −10 dB in the frequency ranges of 12.72–19.53 GHz and 8.96–11.07 GHz, corresponding to the fractional bandwidth of 12.4% and 21.1%, respectively. Here, the LTLP conversion ratio is defined as PCR = $|R_{vu}|^2/(|R_{vu}|^2 + |R_{uu}|^2)$.

The metasurface facilitates efficient LTLP conversion, with its operational frequency being adjustable between the X- and Ku-band, as depicted in Fig. 3c. Simulation results indicate that the PCR achieves 90% in the frequency ranges of 9.03–11.03 GHz and 12.93–19.26 GHz, corresponding to fractional bandwidths of 19.9% and 39.3%, respectively. Notably, the PCR peaks localize at the frequencies of 9.96 GHz, 15.11 GHz, and 18.16 GHz, where the metasurface effectively transforms u-polarized waves into v-polarized waves. Similar performance can also be demonstrated for v-polarized incident waves, with additional explanations provided in Figures S5 and S6 to clarify these results.

Circularly polarized reflected waves can be decomposed into two linearly polarized waves with equal amplitude and a ±90° phase difference. Specifically, the phase difference of +90° results in right-hand-circularly polarized (RHCP) reflected waves, where the electric field vector rotates anti-clockwisely. Conversely, the phase difference of −90° leads to left-hand-circularly polarized (LHCP) reflected waves, characterized by the clockwise rotation of the electric field vector. As illustrated in Figs. 3d and 3e, when the incident azimuth angle is +45°, the metasurface reflects RHCP waves; conversely, when the incident azimuth angle is −45°, it reflects LHCP waves. Based on the phase difference and reflection amplitude in Figs. 3d and 3e, the axial ratio can be calculated as

$$\mathrm{AR} = \sqrt{\frac{R_{vu}^2 + R_{uu}^2 + \sqrt{a}}{R_{vu}^2 + R_{uu}^2 - \sqrt{a}}}, \tag{3}$$

where the parameter a can be described as $a = R_{vu}^4 + R_{uu}^4 + 2(R_{vu}R_{uu})^2 \cos(2\Delta\varphi)$. In practical engineering applications, electromagnetic waves with axial ratios less than 3 dB can be considered as approximately circularly polarized waves. The simulation results presented in Fig. 3f reveal that the reflected waves achieve an axial ratio below 3 dB and exhibit a fractional bandwidth of 32.3% in the frequency range of 14.23–19.72 GHz when the incident azimuth angle is +45°. Conversely, the axial ratio remains below 3 dB with a fractional bandwidth of 30.8% in the frequency range of 14.58–19.89 GHz when the incident azimuth angle is −45°. The above analysis demonstrates that the metasurface can transform linearly polarized incident waves into LHCP or RHCP reflected waves in the Ku- and K-band.

The impact of the oblique incidence angle on the conversion performance of a metasurface is investigated. Figs. 4a and 4b depicting the metasurface in LTLP conversion states illustrate the variation of the PCR along with the variation of the incidence angle. With an increase in the incidence angle, there is a reduction in the PCR bandwidth. This effect is pronounced at lower frequencies, while keeps the stability at higher frequencies. As depicted in Figs. 4a and 4b, the metasurface maintains a PCR exceeding 90% for the incidence angles up to 20° in the PCR bandwidths of 13.18–19.59 GHz with the fractional bandwidth of 39.1% and in the PCR bandwidths of 9.22–11.12 GHz with the fractional bandwidth of 18.7%. Moreover, the correlation between the incident angle and the axial ratio of the proposed metasurface is simulated. Fig. 4c shows that the axial ratio bandwidth also decreases with the increase of the incidence angle. The simulation results of axial ratio exhibit a similar pattern to the PCR, where decline exists at the

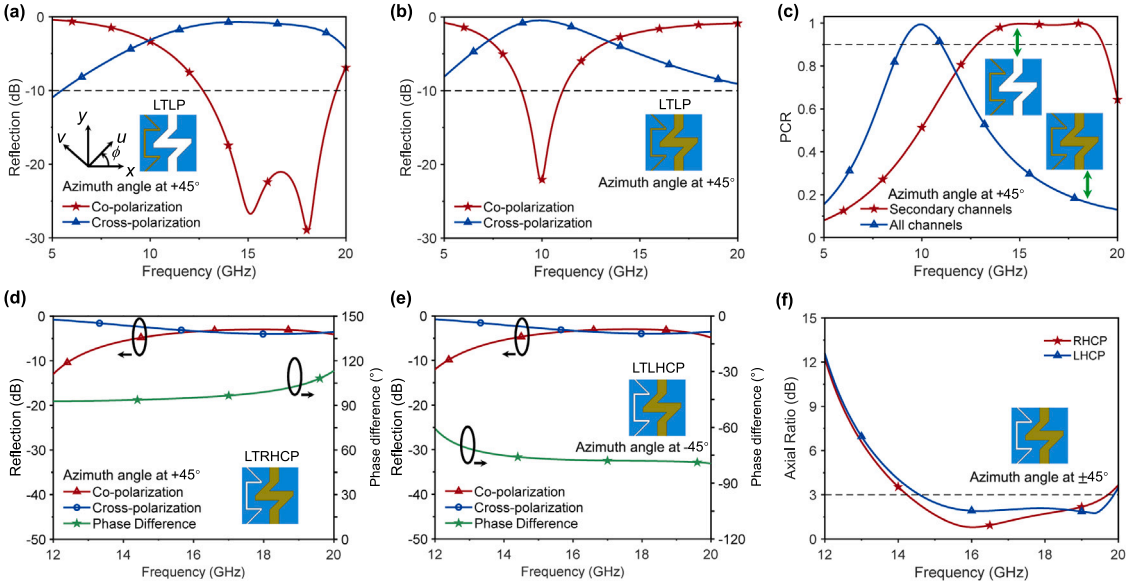

Fig. 3. Simulation results of the metasurface in various polarization conversion states: (a) Amplitudes of the reflection coefficient in the working state 2, with only the secondary microchannels filled with Galinstan. (b) Amplitudes of the reflection coefficient in the working state 3, with all microchannels filled with Galinstan. (c) PCR simulation results for the metasurface in the working states 2 and 3. (d) Amplitudes of the reflection coefficient and phase difference between co-polarized and cross-polarized reflections at an azimuth angle of +45° in the working state 4, with only the main microchannels filled with Galinstan. (e) Amplitudes of the reflection coefficient and phase difference between co-polarized and cross-polarized reflections at an azimuth angle of −45° in the working state 5, with only the main microchannels filled with Galinstan. (f) Axial ratio simulation results for the metasurface in the working states 4 and 5.

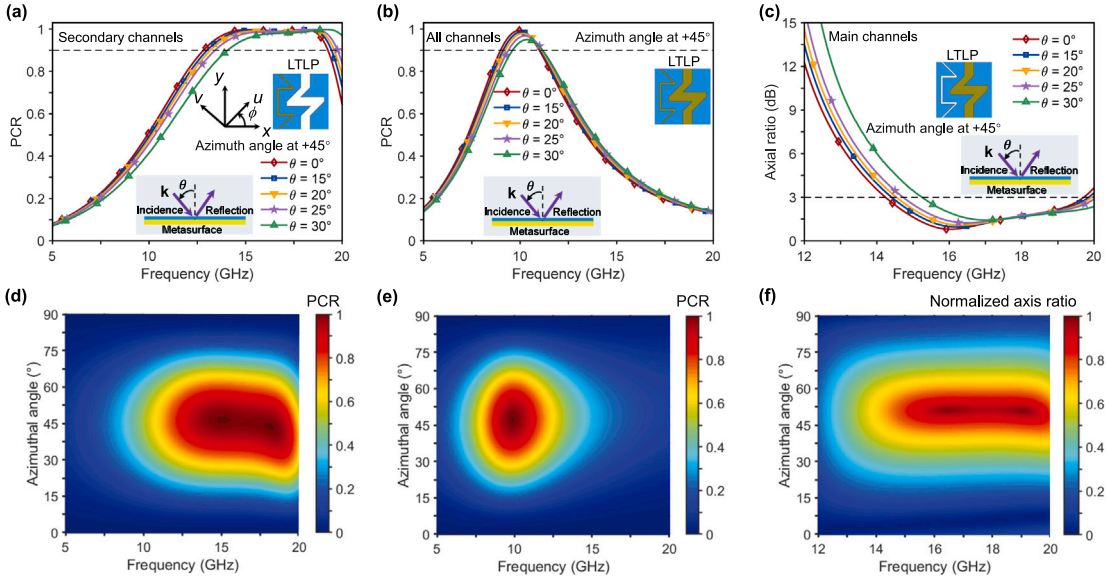

Fig. 4. The effect of the incidence angle θ and azimuthal angle ϕ on polarization conversion. (a) Simulated PCR as a function of frequency and incidence angles for u-polarized incident waves ($\phi = +45°$) in the working state 2. (b) Simulated PCR as a function of frequency and incidence angles for u-polarized incident waves ($\phi = +45°$) in the working state 3. (c) Simulated axial ratio as a function of frequency and incidence angles for u-polarized incident waves ($\phi = +45°$) in the working state 4. (d) Simulated PCR as a function of frequency and azimuthal angles in the working state 2. (e) Simulated PCR as a function of frequency and azimuthal angles in the working state 3. (f) Simulated normalized axial ratio as a function of frequency and azimuthal angles in the working state 4.

lower frequencies for the incidence angles from 0° to 30°. Nevertheless, Fig. 4c demonstrates an insignificant degradation in the axial ratio for incidence angles up to 20°, thereby maintaining a bandwidth with the axial ratio of 3 dB in the frequency range of 14.54–19.94 GHz with the fractional bandwidth of 31.3%.

Figs. 4d–4f show the influence of the incident azimuth angle on the polarization conversion performance of the metasurface. Employing a controlled variable approach, we simulated the polarization conversion performance, where the oblique incidence angle is maintained to be constant, and the incident azimuth angle varies from 0° to 90°. Figs. 4d and 4e illustrate the trends in PCR for working states 2 and 3, respectively. As shown in Fig. 4d, a PCR peak is presented when the incident azimuth angle approaching 45°, signifying near-complete LTLP conversion. As the incident azimuth angle varying around 45°, the corresponding PCR diminishes in an approximately symmetrical fashion. At 15.11 GHz, the PCR consistently exceeds 90% as the incident azimuth angle varying from 37° to 55°. Similar observations exist in Fig. 4e, where the PCR at 9.96 GHz remains larger than 90% throughout the range from 38° to 56° for the incident azimuth angle. In Fig. 4f, a peak of the normalized axial ratio is observed

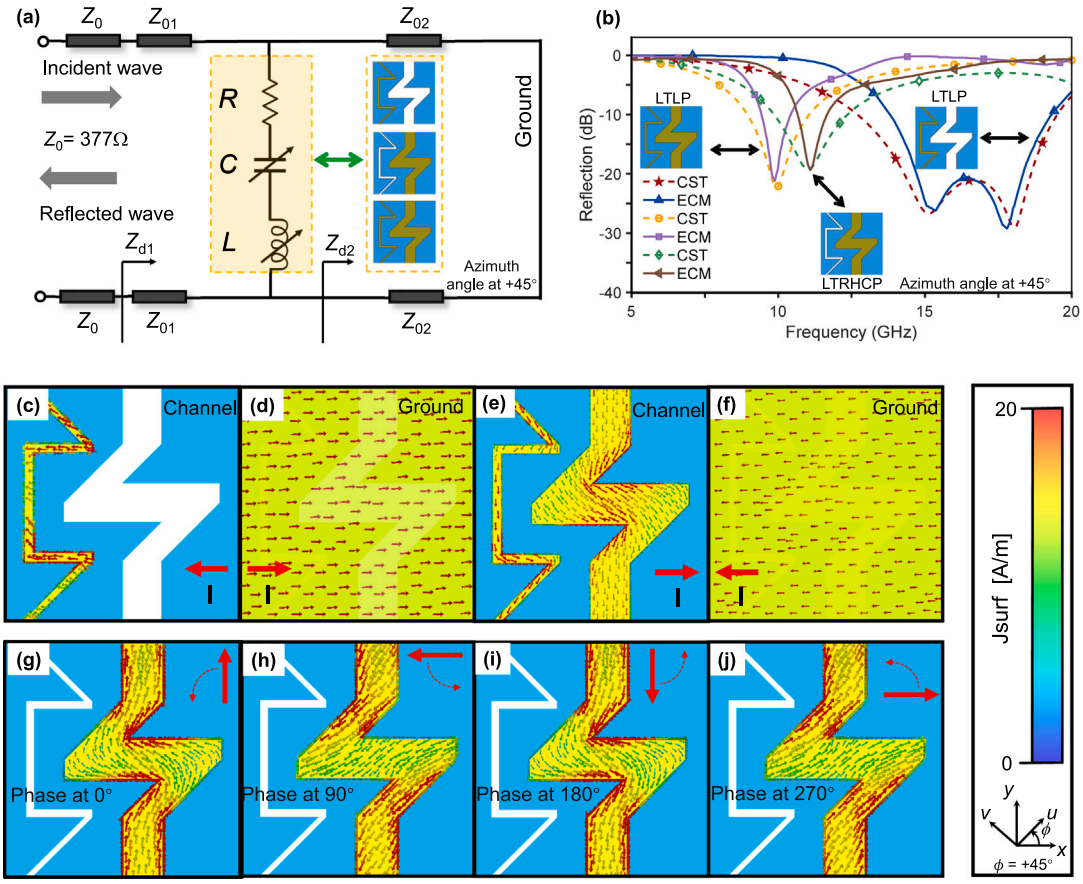

Fig. 5. The equivalent circuit models and the induced surface current density distribution of the metasurface. (a) The RLC circuit model for the metasurface based on the transmission line theory. (b) Comparison of the amplitudes of the reflection coefficient derived from CST and ADS. (c) The microchannel layer distributions at 15.11 GHz in the working state 2. (d) The grounded layer distributions at 15.11 GHz in the working state 2. (e) The microchannel layer distributions at 9.96 GHz in the working state 3. (f) The grounded layer distributions at 9.96 GHz in the working state 3. The induced surface current density distribution in the working state 4, along with its rotational trend. The incident electric field, polarized in the *u*-direction with the incident azimuth angle of +45°, operates at a frequency of 16.9 GHz. (g) Phase at 0°. (h) Phase at 90°. (i) Phase at 180°. (j) Phase at 270°.

when the incident azimuth angle approaches to 50°. As the incident azimuth angle deviates from 50°, the normalized axial ratio begins to diminish in an approximately symmetrical manner. The analysis mentioned above demonstrates that the metasurface is insensitive to the changes in the incidence angle and the incidence azimuth angle in a specific range. These characteristics imply that the metasurface can maintain its performance even when it is conformed to some curved surfaces.

Based on the equivalent circuit theory, the unit cells of electromagnetic metasurfaces involves incorporating continuous metal wire structures, acting as inductors, and metal structures spaced at specific intervals, acting as capacitors, in orthogonal directions. This arrangement induces the phase differences between the two directions to effectively control the phase of the reflected wave. To gain deeper insights into the behaviors of the metasurfaces, we propose the approximate equivalent circuit models, as illustrated in Fig. 5a. Based on the transmission line theory, The impedance of the metasurface can be approximated by the equivalent circuit models (ECM). The structure is grounded, leading to its representation as a short circuit in the equivalent circuit. Additionally, the air and dielectric medium, including PVC and PDMS layers, were modeled by using transmission lines characterized by η_0 and $\eta_0/\sqrt{\varepsilon_r}$. The reflection coefficients can be obtained by using the Advanced Design System (ADS). As depicted in Fig. 5b, the reflection coefficient calculated in ADS is consistent with that simulated in CST.

The preceding analysis establishes a theoretical framework and demonstrates numerical simulation outcomes for metasurface with polarization conversion performance. By analyzing the induced surface current, we can reveal the operational mechanism of the proposed metasurface-based polarization converters. Figs. 5a and 5b illustrate the surface current density distributions on the channel and ground layers when *u*-polarized waves irradiate the metasurface. In the *x*-direction, as shown in Figs. 5a and 5b, the surface currents on the channel and ground layers are inversely parallel at 15.11 GHz, leading to the creation of a magnetic dipole resonance in the *y*-direction. This arrangement significantly increases the equivalent permeability for the electric field in the *y*-direction, thus creating a high impedance surface. As a result, the reflected electric field along the *y*-direction becomes phase-inverted. Conversely, in the *x*-direction, the absence of dipole resonance ensures that the reflected electric field remains in phase with the incident electric field. This phenomenon results in a *v*-polarized synthesized reflected field at 15.11 GHz. Figs. 5c and 5d reveal that the currents on the channel and ground layers at 9.96 GHz are anti-parallel in the *x*-direction, generating the magnetic dipole resonance in the *y*-direction. Therefore, the resultant reflected electric field is *v*-polarized.

To further elucidate the physical mechanism of the working state 4, Figs. 5g–5j illustrate the induced surface current distribution on the upper surface of the main channels, which are filled with liquid metal. For the *u*-polarized incident electric field (ϕ = +45°), it is observed that the surface current vectors rotate counter-clockwisely as the time

Table 2
Comparisons of the proposed design with other polarization converters.

Ref.	Working mode	Center frequency [GHz]	Functions	Bandwidth	Unit size (λ_0)	Tunable elements
[19]	Reflection	6.55, 5.90	LTRHCP, LTLP	50.38%, 67.80%	0.32×0.32	1 Varactor
[20]	Reflection	4.20	LTLP	38.57%	0.34×0.34	2 PINs
[21]	Transmission	9.82	LTRHCP, LTLHCP	2.34%	0.49×0.49	4 PINs
[22]	Transmission	14.55	LTLHCP	6.19%	0.38×0.61	1 PIN
[23]	Transmission	10.95	LTLP	105.02%	0.21×0.21	4 PINs
[24]	Transmission	5.75	LTLP	60.80%	0.38×0.38	6 PINs
[25]	Reflection	5.50	LTLP	25.45%	0.17×0.17	4 PINs
[26]	Reflection	10.25, 9.07	LTLP, LTRHCP	51.7%, 29.22%	0.36×0.36	1 MEMS
This work	Reflection	16.10, 10.03, 17.24, 16.98	LTLP, LTRHCP, LTLHCP	37.66%, 14.60%, 30.30%, 30.20%	0.32×0.32	Liquid metal

phase varies from 0° to 270°. From Figs. 5g–5j, it can be further confirmed that the metasurface can convert *u*-polarized incident waves into RHCP reflected waves in the working state 4. Similarly, owing to the rotational symmetry of the main channel structure, the metasurface can convert *v*-polarized incident waves ($\phi = -45°$) into LHCP reflected waves in the working state 5.

3. Fabrication and experimental results

As shown in Table 2, reconfigurable polarization converters provided in the existing references primarily utilize MEMS-based switches or DC bias elements such as varactors and PIN diodes. In contrast, our study employs a liquid metal microfluidic system to achieve reconfiguration. Comparing our metasurface with the references in Table 2 reveals that metasurfaces integrating varactor or PIN diodes exhibit limited operational states. They struggle to convert incident waves into arbitrary polarization states for either transmitted or reflected waves, with a concentration around specific central frequencies, thus limiting their potential cross-band applications. To overcome these challenges, we designed and fabricated a reconfigurable metasurface based on liquid metal, testing its polarization conversion capabilities in a microwave anechoic chamber. We integrated multiple microchannels within a single unit of the metasurface, offering significant advantages in enhancing the versatility of reconfigurable metasurfaces. In this study, we successfully implemented multiple functionalities, including LTLP, LTLHCP, and LTRHCP conversions in the X- and Ku-band, using only two types of microchannels.

We integrated a metasurface unit containing multiple microchannels into a single-layer structure, which not only reduces the overall device thickness and manufacturing complexity but also facilitates the development of higher integration polarization conversion devices. Leveraging the excellent fluidity of liquid metal, we can flexibly control its integration or separation with microchannels. For instance, in working state 1, liquid metal acts as a polarization conversion switch, enabling the metasurface to maintain the polarization state of incident waves, a capability that traditional solid-metal-based metasurfaces struggle to achieve. The use of flexible materials such as PDMS presents potential opportunities for conformal applications of reconfigurable metasurface devices. This approach facilitates a wider array of polarization conversion functions without requiring complex bias circuits, thus enhancing the efficiency of the overall circuit design process. Additionally, electronic control modulates the electromagnetic response of metasurfaces by adjusting the port voltage (forward or reverse) of the diodes. In contrast, the advantage of reconfigurable metasurfaces based on liquid metal is that they can flexibly design the structure and distribution of microchannels and control their injection state in microchannels in combination with liquid metal microfluidic technology to meet the requirement of diverse applications.

To evaluate the performance of the microfluidic metasurface, we fabricated and characterized a 20 × 20 elements polarizer array. The experimental setup, illustrated in Fig. 6, utilized a receive antenna and a transmit antenna. The fabricated sample, as depicted in Fig. 6b, had overall dimensions of $140 \times 160 \times 4.4\,\text{mm}^3$. The microfluidic channels were fabricated by using laser to etch a PVC substrate with the thickness of 0.7 mm. Liquid metal tends to form an oxide layer when exposed to air, which adheres to the inner walls of the microchannels, thereby limiting reconfiguration. Consequently, prior to injecting the liquid metal, a 0.5 M NaOH solution was introduced into the microchannel to remove the oxide residue. PVC was chosen as the substrate material due to its low dielectric loss and stability, which ensured that it did not interfere with the electromagnetic response of the metasurface. To provide mechanical resilience and support, we used a 3 mm-thick layer of PDMS, a commonly used elastomer known for its mechanical flexibility and electrical insulating properties. We assembled the layers into a multilayer structure by using pressure sensitive adhesive for bonding to ensuring both the mechanical flexibility and electromagnetic functionality of the metasurface. The performance of the metasurface was evaluated by using the free-space technique. A vector network analyzer (VNA) was utilized, with two horn antennas connected to it for transmitting and receiving electromagnetic waves. The amplitudes of the reflection coefficients were measured for co-polarization and cross-polarization in the frequency range of 4–20 GHz. Rotating both the transmitting and receiving horn antennas allows for the acquisition of various incident azimuth angles, enabling the measurement of S-parameters. Furthermore, a reference measurement of the co-polarization reflection coefficient was implemented by using the ground plane of the sample.

In working state 1, the metasurface serves as a reflector irradiated by the linearly polarized incident waves. Fig. 6d illustrates the measured and simulated values of the amplitudes of the co-polarized and cross-polarized reflection coefficients in the frequency range of 8–12 GHz. Fig. 6 demonstrates that no polarization conversion occurs when both types of the channels are empty, where the cross-polarized reflection coefficient R_{vu} is significantly lower than the co-polarized reflection coefficient R_{uu}. The comparison between simulation and measurement results also highlights the influence of the finite number of unit cells. The difference between the cross-polarized reflection (approximately −35 dB) in the X-band for the finite sample size and the simulated infinite metasurface (below −45 dB) can be attributed to the limited dimensions of the fabricated metasurface, as well as manufacturing errors, dielectric losses from the pressure sensitive adhesive used in fabrication, and a small residue of sodium hydroxide solution in the channels.

In working state 2 and 3, the measured PCR results presented in Fig. 6e, indicate that the *u*-polarized incident waves can be converted to *v*-polarized reflected waves in the frequency ranges of 12.76–18.68 GHz and 9.39–10.82 GHz, with the PCR larger than 90%. The discrepancies between the measured and simulated results may arise from the fabrication and measurement tolerances. For instance, electromagnetic property of the pressure sensitive adhesive used in the metasurface assembly were not included in the simulation. These practical factors introduce the variations between the predicted and measured results, where the deviation is acceptable.

In working state 4 and 5, the metasurface operates in the LTC polarization conversion state. The calculated values of the axial ratio derived are displayed in Fig. 6f. The empirical results affirm that the LTRHCP and LTLHCP conversion states can achieve the 3 dB axial ratio

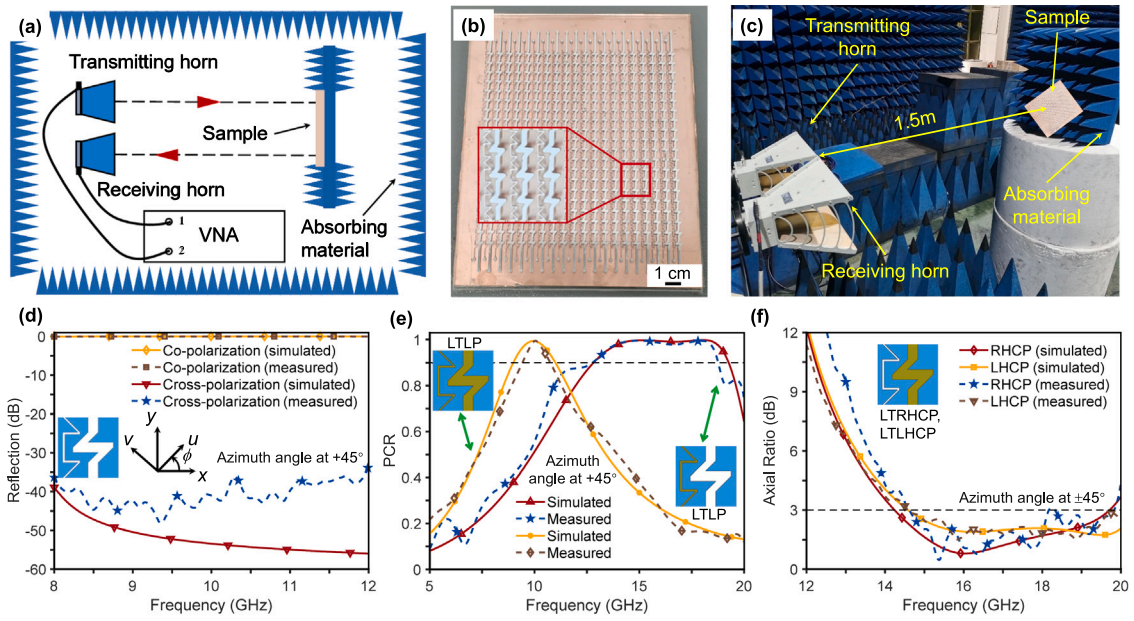

Fig. 6. Measurement setup and the test results of the metasurface. (a) Sketch of the measuring platform. (b) Photograph of the fabricated sample. (c) Configuration of the measurement setup. (d) Simulated and measured amplitudes of the reflection coefficient for the metasurface in the reflection state in the case of *u*-polarized incident waves. (e) Simulated and measured PCR results in the LTLP conversion states. (f) Simulated and measured axial ratio results in the linear-to-circular polarization conversion states.

bandwidth in the frequency ranges of 14.61–19.83 GHz with the fractional bandwidth of 30.3% and 14.57–19.76 GHz with the fractional bandwidth of 30.2%. The measured results of the metasurface in the LTC polarization conversion configuration exhibit good agreement with the simulated results. However, some divergence is observed between the measured and simulated for the 3 dB axial ratio bandwidth. This discrepancy originates from the factors such as finite sample size, fabrication tolerances, and constraints inherent in the measurement setup. In the experiments, large size of the metasurface yield better consistency with the simulated results. The presence of these practical aspects inevitably introduces the variations that may slightly deviate from the ideal simulated scenario.

4. Conclusions

In conclusion, this paper presents a metasurface based on liquid metal that achieves multifunctional polarization conversion by integrating various types of microchannels on a single layer. The integration of different types of microchannels allows for enhanced functionality and flexibility in manipulating polarization states. By modifying the filling mode of the liquid metal, the metasurface can generate different reflected waves across various frequency bands. The reflected waves are linearly polarized in the X- and Ku-band with the fractional bandwidths of 14.60% and 37.66%, respectively. And it can produce circularly polarized waves in the Ku- and K-band with the fractional bandwidths of 30.30% and 30.20%, respectively. Overall, the microfluidics of liquid metal presents new opportunities for polarization conversion, allowing for more versatile and efficient metasurface designs, free from some of the drawbacks associated with the previous reconfigurable methods. The multifunctional polarization converter metasurface offers prospects for the applications of microwave imaging, remote sensing, communication systems, etc.

CRediT authorship contribution statement

Shibo Gao: Writing – original draft, Conceptualization. **Bowen Li:** Software. **Yu Lin:** Methodology. **Yanan Shao:** Software. **Yongting Deng:** Supervision. **Jan G. Korvink:** Supervision. **Yongbo Deng:** Supervision.

Declaration of competing interest

The authors declare that they have no known competing financial interests or personal relationships that could have appeared to influence the work reported in this paper.

Acknowledgments

This work was mainly supported by the National Natural Science Foundation of China (No. 51875545), Science and Technology Development Plan of Jilin Province, China (No. SKL202302020), CAS Project for Young Scientists in Basic Research, China (No. YSBR-066), the Innovation Grant of Changchun Institute of Optics, Fine Mechanics and Physics (CIOMP), China, EU2020 FET grant (TiSuMR, 737043), the DFG, Germany under grant KO 1883/20-1 Metacoils, funding within their framework of the German Excellence Intitiative under grant EXC 2082 “3D Matter Made to Order”, and from the VirtMat initiative “Virtual Materials Design”.

Appendix A. Supplementary data

Supplementary material related to this article can be found online at https://doi.org/10.1016/j.optcom.2024.131339.

Data availability

Data will be made available on request.

References

[1] Alex M.H. Wong, George V. Eleftheriades, Perfect anomalous reflection with a bipartite huygens’ metasurface, Phys. Rev. X 8 (1) (2018) 011036.
[2] Zhenci Sun, Chao Liang, Chen Chen, Xiayu Wang, Enze Zhou, Xiaomeng Bian, Yuanmu Yang, Rui You, Xiaoguang Zhao, Jiahao Zhao, et al., High-efficiency dynamic terahertz deflector utilizing a mechanically tunable metasurface, Research 6 (2023) 0274.
[3] Stanislav B. Glybovski, Sergei A. Tretyakov, Pavel A. Belov, Yuri S. Kivshar, Constantin R. Simovski, Metasurfaces: From microwaves to visible, Phys. Rep. 634 (2016) 1–72.

[4] Sergejs Boroviks, Rucha A. Deshpande, N. Asger Mortensen, Sergey I. Bozhevolnyi, Multifunctional metamirror: polarization splitting and focusing, Acs Photonics 5 (5) (2017) 1648–1653.
[5] Zhongyi Guo, Lie Zhu, Fei Shen, Hongping Zhou, Rongke Gao, Dielectric metasurface based high-efficiency polarization splitters, RSC Adv. 7 (16) (2017) 9872–9879.
[6] Mohammadreza Khorasaninejad, Francesco Aieta, Pritpal Kanhaiya, Mikhail A. Kats, Patrice Genevet, David Rousso, Federico Capasso, Achromatic metasurface lens at telecommunication wavelengths, Nano Lett. 15 (8) (2015) 5358–5362.
[7] Wei Ting Chen, Alexander Y Zhu, Vyshakh Sanjeev, Mohammadreza Khorasaninejad, Zhujun Shi, Eric Lee, Federico Capasso, A broadband achromatic metalens for focusing and imaging in the visible, Nature Nanotechnol. 13 (3) (2018) 220–226.
[8] B. Zheng, I. Yamashita, M. Uenuma, K. Iwahori, M. Kobayashi, Y. Uraoka, Site-directed delivery of ferritin-encapsulated gold nanoparticles, Nanotechnology 21 (4) (2009) 045305.
[9] J.P. Balthasar Mueller, Noah A. Rubin, Robert C. Devlin, Benedikt Groever, Federico Capasso, Metasurface polarization optics: independent phase control of arbitrary orthogonal states of polarization, Phys. Rev. Lett. 118 (11) (2017) 113901.
[10] Chunsheng Guan, Jian Liu, Xumin Ding, Zhuochao Wang, Kuang Zhang, Haoyu Li, Ming Jin, Shah Nawaz Burokur, Qun Wu, Dual-polarized multiplexed meta-holograms utilizing coding metasurface, Nanophotonics 9 (11) (2020) 3605–3613.
[11] Zhuochao Wang, Guangwei Hu, Xinwei Wang, Xumin Ding, Kuang Zhang, Haoyu Li, Shah Nawaz Burokur, Qun Wu, Jian Liu, Jiubin Tan, et al., Single-layer spatial analog meta-processor for imaging processing, Nat. Commun. 13 (1) (2022) 2188.
[12] Qingze Tan, Bin Zheng, Tong Cai, Chao Qian, Rongrong Zhu, Xiaofeng Li, Hongsheng Chen, Broadband spin-locked metasurface retroreflector, Adv. Sci. 9 (20) (2022) 2201397.
[13] Weixu Yang, Ke Chen, Yilin Zheng, Wenbo Zhao, Qi Hu, Kai Qu, Tian Jiang, Junming Zhao, Yijun Feng, Angular-adaptive reconfigurable spin-locked metasurface retroreflector, Adv. Sci. 8 (21) (2021) 2100885.
[14] Yao-Wei Huang, Wei Ting Chen, Wei-Yi Tsai, Pin Chieh Wu, Chih-Ming Wang, Greg Sun, Din Ping Tsai, Aluminum plasmonic multicolor meta-hologram, Nano Lett. 15 (5) (2015) 3122–3127.
[15] Nanfang Yu, Federico Capasso, Flat optics with designer metasurfaces, Nat. Mater. 13 (2) (2014) 139–150.
[16] H.L. Zhu, S.W. Cheung, X.H. Liu, T.I. Yuk, Design of polarization reconfigurable antenna using metasurface, IEEE Trans. Antennas Propagat. 62 (6) (2014) 2891–2898.
[17] Long Li, Yongjiu Li, Zhao Wu, Feifei Huo, Yongliang Zhang, Chunsheng Zhao, Novel polarization-reconfigurable converter based on multilayer frequency-selective surfaces, Proc. IEEE 103 (7) (2015) 1057–1070.
[18] Badreddine Ratni, André de Lustrac, Gérard-Pascal Piau, Shah Nawaz Burokur, Electronic control of linear-to-circular polarization conversion using a reconfigurable metasurface, Appl. Phys. Lett. 111 (21) (2017).
[19] Xi Gao, Wan Li Yang, Hui Feng Ma, Qiang Cheng, Xin Hua Yu, Tie Jun Cui, A reconfigurable broadband polarization converter based on an active metasurface, IEEE Trans. Antennas and Propagation 66 (11) (2018) 6086–6095.
[20] Shangyi Sun, Wen Jiang, Shuxi Gong, Tao Hong, Reconfigurable linear-to-linear polarization conversion metasurface based on PIN diodes, IEEE Antennas Wirel. Propag. Lett. 17 (9) (2018) 1722–1726.
[21] Xiaoliang Ma, Wenbo Pan, Cheng Huang, Mingbo Pu, Yanqin Wang, Bo Zhao, Jianhua Cui, Changtao Wang, Xiangang Luo, An active metamaterial for polarization manipulating, Adv. Opt. Mater. 2 (10) (2014) 945–949.
[22] Wei Li, Song Xia, Bin He, Jianzhong Chen, Hongyu Shi, Anxue Zhang, Zhenrong Li, Zhuo Xu, A reconfigurable polarization converter using active metasurface and its application in horn antenna, IEEE Trans. Antennas and Propagation 64 (12) (2016) 5281–5290.
[23] You Li, Qunsheng Cao, Yi Wang, A wideband multifunctional multilayer switchable linear polarization metasurface, IEEE Antennas Wirel. Propag. Lett. 17 (7) (2018) 1314–1318.
[24] Chen Zhang, Jun Gao, Xiangyu Cao, Si-Jia Li, Huanhuan Yang, Tong Li, Multifunction tunable metasurface for entire-space electromagnetic wave manipulation, IEEE Trans. Antennas and Propagation 68 (4) (2019) 3301–3306.
[25] Michal Cerveny, Kenneth Lee Ford, Alan Tennant, Reflective switchable polarization rotator based on metasurface with PIN diodes, IEEE Trans. Antennas and Propagation 69 (3) (2020) 1483–1492.
[26] Huicun Yu, Xiangyu Cao, Jun Gao, Huanhuan Yang, Liaori Jidi, Jiangfeng Han, Tong Li, Design of a wideband and reconfigurable polarization converter using a manipulable metasurface, Opt. Mater. Express 8 (11) (2018) 3373–3381.
[27] Yuan Hsing Fu, Ai Qun Liu, Wei Ming Zhu, Xu Ming Zhang, Din Ping Tsai, Jing Bo Zhang, Ting Mei, Ji Fang Tao, Hong Chen Guo, Xin Hai Zhang, et al., A micromachined reconfigurable metamaterial via reconfiguration of asymmetric split-ring resonators, Adv. Funct. Mater. 21 (18) (2011) 3589–3594.
[28] Wei Ming Zhu, Ai Qun Liu, Xu Ming Zhang, Din Ping Tsai, Tarik Bourouina, Jing Hua Teng, Xin Hai Zhang, Hong Chen Guo, Hendrix Tanoto, Ting Mei, et al., Switchable magnetic metamaterials using micromachining processes, Adv. Mater. 23 (15) (2011) 1792.
[29] Y.J. Yoo, S. Ju, S.Y. Park, Y.J. Kim, J. Bong, T. Lim, K.W. Kim, J.Y. Rhee, Y. Lee, Metamaterial absorber for electromagnetic waves in periodic water droplets sci, Rep 5 (2015) 14018.
[30] Weiming Zhu, Qinghua Song, Libin Yan, Wu Zhang, Pin-Chieh Wu, Lip Ket Chin, Hong Cai, Din Ping Tsai, Zhong Xiang Shen, Tian Wei Deng, et al., A flat lens with tunable phase gradient by using random access reconfigurable metamaterial, Adv. Mater. 27 (32) (2015) 4739–4743.
[31] Xin Yu Wu, Hong Yuan Feng, Fengshuo Wan, Meng Wei, Chong Guo, Longzhu Cai, Fan Wu, Zhi Hao Jiang, Lei Kang, Wei Hong, et al., An ultrathin, fast-response, large-scale liquid-crystal-facilitated multi-functional reconfigurable metasurface for comprehensive wavefront modulation, Adv. Mater. (2024) 2402170.
[32] Libin Yan, Weiming Zhu, Muhammad Faeyz Karim, Hong Cai, Alex Yuandong Gu, Zhongxiang Shen, Peter Han Joo Chong, Dim-Lee Kwong, Cheng-Wei Qiu, Ai Qun Liu, 0.2 λ0 thick adaptive retroreflector made of spin-locked metasurface, Adv. Mater. 30 (39) (2018) 1802721.
[33] Pin Chieh Wu, Weiming Zhu, Zhong Xiang Shen, Peter Han Joo Chong, Wee Ser, Din Ping Tsai, Ai-Qun Liu, Broadband wide-angle multifunctional polarization converter via liquid-metal-based metasurface, Adv. Opt. Mater. 5 (7) (2017) 1600938.
[34] Ololade M. Sanusi, Ying Wang, Langis Roy, Reconfigurable polarization converter using liquid metal based metasurface, IEEE Trans. Antennas and Propagation 70 (4) (2021) 2801–2810.